










Search for large topological gaps in atomic spin chains on proximitized superconducting heavy-metal layers

Philip Beck ^{1,7}, Bendegúz Nyári ^{2,3,7}, Lucas Schneider¹, Levente Rózsa ^{3,4,5}, András Lászlóffy ⁵, Krisztián Palotás ^{3,5,6}, László Szunyogh ^{2,3}, Balázs Ujfalussy ⁵✉, Jens Wiebe ¹✉ & Roland Wiesendanger ¹

One-dimensional systems comprising *s*-wave superconductivity with meticulously tuned magnetism realize topological superconductors hosting Majorana modes whose stability is determined by the gap size. However, for atomic spin chains on superconductors, the effect of the substrate's spin-orbit coupling on the topological gap is largely unexplored. Here, we introduce an atomic layer of the heavy metal gold on a niobium surface combining strong spin-orbit coupling and a large superconducting gap with a high crystallographic quality, enabling the assembly of defect-free iron chains using a scanning tunneling microscope tip. Scanning tunneling spectroscopy experiments and density functional theory calculations reveal ungapped Yu-Shiba-Rusinov bands in the ferromagnetic chain despite the heavy substrate. By artificially imposing a spin spiral state, the calculations indicate minigap opening and zero-energy edge state formation. The methodology enables a material screening of heavy-metal layers on elemental superconductors for ideal systems hosting Majorana edge modes protected by large topological gaps.

¹Department of Physics, University of Hamburg, Jungiusstrasse 9A, 20355 Hamburg, Germany. ²ELKH-BME Condensed Matter Research Group, Budapest University of Technology and Economics, Műegyetem rkp. 3., H-1111 Budapest, Hungary. ³Department of Theoretical Physics, Institute of Physics, Budapest University of Technology and Economics, Műegyetem rkp. 3., H-1111 Budapest, Hungary. ⁴Department of Physics, University of Konstanz, D-78457 Konstanz, Germany. ⁵Wigner Research Centre for Physics, Institute for Solid State Physics and Optics, H-1525 Budapest, Hungary. ⁶ELKH-SZTE Reaction Kinetics and Surface Chemistry Research Group, University of Szeged, H-6720 Szeged, Hungary. ⁷These authors contributed equally: Philip Beck, Bendegúz Nyári. ✉email: ujfalussy.balazs@wigner.hu; jwiebe@physnet.uni-hamburg.de

Inducing spin-orbit coupling (SOC) in nanostructures has recently been of great interest in a variety of disciplines related to surface science¹ due to its close ties with the existence of non-collinear magnetic states^{2–4}, spin-split surface states^{5,6}, topological surface states^{7,8} and topological superconductivity^{9–11} which can be accompanied by Majorana bound states (MBS)^{12–19}. Since the latter is a promising candidate as a building block of topological quantum computers²⁰, systems which may potentially host MBS have attracted a lot of interest. MBS may be realized in chains of magnetic atoms, also called atomic spin chains, on *s*-wave superconductors^{14,15,19,21–23}, artificially fabricated by atom manipulation with the tip of a scanning tunneling microscope (STM)²⁴. Although first experimental realizations, e.g., Fe chains on Re(0001), show signatures of MBS in scanning tunneling spectroscopy (STS)¹⁹, the system suffers from the small energy gap Δ_s of the superconducting rhenium substrate, making a clear allocation of in-gap features difficult²¹. More recent results of such atomic spin chains on Nb(110)^{25–27} circumvent this, but presumably at the price of lower SOC, which manifests itself in the dominance of collinear magnetic ground states due to weak Dzyaloshinskii–Moriya interaction (DMI) terms²⁸, and the hybridization of the spatially extended precursors of MBS in experimentally accessible chain lengths²⁶.

Aiming at maintaining the largest gap $\Delta_s = 1.50$ meV of all elemental superconductors combined with the possibility of atom manipulation which the Nb substrate offer, there are two apparent approaches to induce a higher SOC in the system. On the one hand, one may think of using atoms with larger atomic SOC, e.g. rare-earth metals, for the formation of the atomic spin chain. On the other hand, one can try to couple the chain to a heavy-metal substrate with potentially larger SOC, which is grown on Nb(110) and therefore becomes superconducting by proximity. First attempts combining both approaches using Gd atoms on bismuth thin films grown on Nb(110) show hybridization of the Yu–Shiba–Rusinov (YSR) states of small ensembles of 3–4 Gd atoms²⁹. However, the assembly of longer chains and a formation of bands from the hybridizing YSR states, which are both prerequisites for the emergence of topological superconductivity and MBS, were not possible for that system. Moreover, it is even unclear whether a larger SOC in the constituents, i.e., chain, substrate, or both of them, will lead to a larger SOC in the YSR bands of the hybrid chain system which is finally relevant for the emergence of topological superconductivity with a large topological gap and well-defined MBS isolated at the ends of the chain.

Here, we investigate these questions by pursuing the second approach by constructing Fe chains on ultrathin Au films grown on Nb(110) used as a substrate. Au is well known to exhibit large SOC^{5,30} and the proximity to Au has been demonstrated to enhance SOC-induced effects in light elements, including the scattering rate³¹, the Rashba spin-splitting^{32,33}, and also the magnetocrystalline anisotropy energy³⁴. Moreover, twisted spin textures were predicted to occur around single Fe atoms³⁵ and in Mn chains³⁶ on Au(111). Tens of monolayers (ML) thick Au films grown on superconducting vanadium show energy gaps demonstrating that the Au becomes superconducting by proximity³⁷. Since previous low-energy electron diffraction (LEED) studies hint at the possibility to grow pseudomorphic thin films of Au on Nb(110)³⁸, it is a natural candidate to be used as a proximitized superconducting heavy-metal layer on Nb(110). Combining experimental STS and density functional theory (DFT) calculations by solving the fully relativistic Dirac–Bogoliubov–de Gennes (DBdG) equations of the single Fe adatom, dimers and chains, we study (i) whether there is indeed a topological gap opening in the YSR bands due to the large SOC in the Au substrate, and (ii) the effect of a different spin structure in

the chain on the topological gap width and the localization of MBS.

Results and discussion

Monolayer Au on Nb(110). We first describe the growth and the superconducting properties of the heavy-metal layer. We aimed at the preparation of ultrathin Au films, maintaining the surface structure of Nb(110) as it offers multiple distinct building directions for artificial chains, which enables some tuning of the hybridization of YSR states^{28,39,40} and, therefore, of the in-gap band structure of such chains^{25,26}. An overview STM image of the Au/Nb(110) sample after the low-temperature deposition of Fe atoms is shown in Fig. 1a (preparation details in the Methods section). The Nb(110) surface is almost completely covered by one monolayer of Au (see sketch in Fig. 1a), with only a few remaining holes. Pseudomorphic growth, as predicted by LEED studies³⁸, is confirmed by manipulated atom STM images⁴¹ (Supplementary Note 1 and Supplementary Fig. 1) of the first monolayer. Partially, the second monolayer Au has started to grow at step edges and in the form of a few free-standing islands (Fig. 1b). In this ultrathin limit, we find that the energy gap of the superconducting Nb is fully preserved in the monolayer Au due to the proximity effect, as demonstrated by the deconvoluted dI/dV spectrum (see Methods and Supplementary Note 2 for the deconvolution procedure) taken on the bare monolayer Au on Nb(110) far from any Fe atom in Fig. 1c (gray curve). The energy gap on the monolayer Au is of equal size as that of bare Nb(110) at our measurement temperature and the in-gap dI/dV signal is zero (see Supplementary Fig. 2). This behavior is crucial for our experiments, but might be altered for thicker films as indicated by recent theoretical^{42,43} and experimental^{44,45} studies.

YSR states of single Fe atoms. We continue with the investigation of the YSR states induced by single Fe atoms, i.e., the building blocks of chains. According to our DFT calculations, the Fe adatom has a magnetic moment of $3.57\mu_B$ with a preferred orientation perpendicular to the Au surface (Supplementary Note 5). A close-up STM image of the statistically distributed single Fe adatoms is shown in Fig. 1b, where they appear as shallower protrusions on the first monolayer and as brighter spheres on the second monolayer. We restrict ourselves to the first monolayer since only this layer has large enough terraces to construct artificial chains. The Fe adatoms are adsorbed on the fourfold coordinated hollow sites on this monolayer Au (Supplementary Note 1 and Supplementary Fig. 1). Fe adatoms which are adsorbed far from other adatoms or defects show similar dI/dV spectra as shown in Fig. 1c (red curve). This reproducibility is required for a well-defined band formation in bottom-up fabricated nanostructures made from such individual adatoms. On the adatoms we find two pairs of YSR states induced in the gap of the Au monolayer which are marked by black arrows and Greek letters^{46–48}. One of them is energetically located close to the Au monolayer gap edge ($\pm\alpha$, ± 1.23 meV) while the other one is located close to the Fermi energy E_F ($\pm\beta$, ± 0.27 meV). We use constant-contour maps (see Methods) to resolve the spatial distribution of both YSR states^{47,48}, as shown in Fig. 1d. The $\pm\alpha$ state has a spatial distribution resembling that of a d_{yz} orbital with two lobes pointing along the $[1\bar{1}0]$ direction. On the other hand, a spatial distribution resembling that of a d_{xz} orbital extended along the $[001]$ direction is observed for the $\pm\beta$ state. Note that the shapes of the $+\beta$ and the $-\beta$ state are somewhat different since the former has additional faint lobes along the $[1\bar{1}0]$ direction probably indicating contributions from a $d_{x^2-y^2}$ -like YSR state. The spatial distributions are explainable by the orbital origin of YSR states^{28,47,48} and the point group C_{2v} for the system.

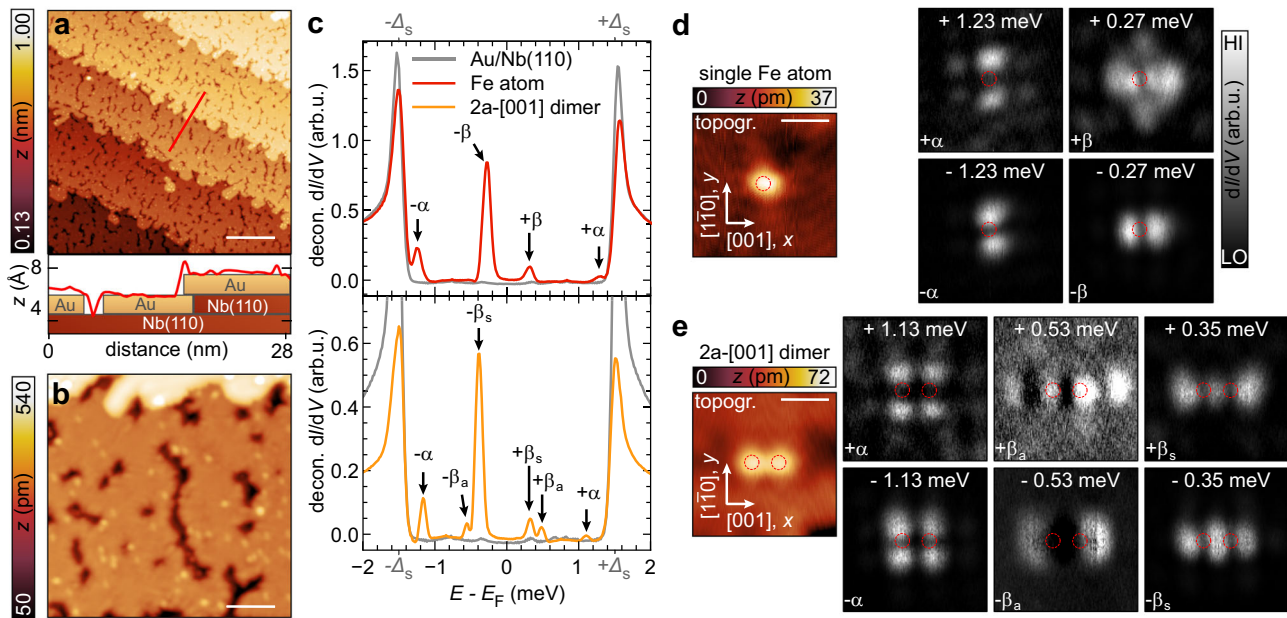


Figure 1 Measured Yu-Shiba-Rusinov (YSR) states of Fe atoms and dimers on monolayer Au on Nb(110). **a** Scanning tunneling microscope (STM) image of an ultrathin film of Au on Nb(110) with an approximate coverage of 1 monolayer Au and additionally deposited Fe atoms. An extracted line profile along the red line is displayed underneath (red curve). Rectangles show the surface composition underneath the line profile. The white scale bar has a length of 20 nm ($V_{\text{bias}} = 50$ mV and $I = 100$ pA). **b** STM image of randomly distributed Fe atoms on 1 monolayer Au (bottom part of the image) and 2 monolayer Au (topmost part of the image). The white scale bar has a length of 4 nm ($V_{\text{bias}} = 6$ mV and $I = 3$ nA). **c** Deconvoluted dI/dV spectra (decon. dI/dV in arbitrary units, arb. u.) measured on the Au/Nb(110) substrate (gray), a single Fe atom (red), and the center of a dimer of Fe atoms spaced by $2a$ along the [001] direction (orange). Black arrows and Greek letters label YSR states. Gray ticks mark the position of the superconducting energy gap of the sample $\Delta_s = 1.50$ meV as determined in Supplementary Note 2 ($V_{\text{stab}} = 6$ mV, $I_{\text{stab}} = 1$ nA and $V_{\text{mod}} = 20$ μ V). **d, e** STM images (colored images named topogr.) and constant-contour maps (grayscale images) of a single Fe atom (**d**) and a Fe dimer (**e**) spaced by $2a$ along the [001] direction. Constant-contour maps were obtained for every energy for which we identified a peak in the corresponding spectrum of (**c**) as indicated by the corresponding Greek letters. White arrows indicate crystallographic directions, red dashed circles depict the positions of the Fe atoms as determined from the topographies (topogr.), and white scale bars represent a length of 1 nm ($V_{\text{bias}} = 6$ mV and $I = 1$ nA).

However, note that the energetic order of the states is interchanged with respect to the case of bare Nb(110)²⁸, and that there are no obvious indications for the other two possible, d_{xy} - and d_{z^2} -like, YSR states, which might indicate an overlap of these peaks in energy with the d_{xz} -, d_{yz} -, or $d_{x^2-y^2}$ -like YSR states, or that they are hidden in the coherence peaks of the substrate.

In order to further clarify these experimental results we calculated the local density of states (LDOS) for a single Fe atom on the Au/Nb(110) film as shown in the red curve of Fig. 2a and in Fig. 2b (see Methods for the calculation details). There are three very close, almost overlapping YSR states in the vicinity of the substrate's coherence peaks (see also Supplementary Fig. 5a). They correspond to the d_{z^2} , d_{xy} and d_{yz} orbitals (see the $+1.32$ meV map in Fig. 2b) and the spatial distributions of the LDOS around these peaks are very sensitive to the exact energy (Supplementary Fig. 5b). Due to their energetic location and orbital symmetries, we assign them to the experimental $\pm\alpha$ YSR state (cf. Fig. 1c and d) which appear as a single peak in the dI/dV spectrum due to the finite-temperature smearing. Additionally, there are two most intense peaks in the calculations which stem from two energetically close YSR states near E_F where the one closest to E_F corresponds to the $d_{x^2-y^2}$ orbital (see the $+0.38$ meV map in Fig. 2b), and the less intense one further apart from E_F to the d_{xz} orbital (see the -0.58 meV map in Fig. 2b). While the latter resembles the experimentally observed $-\beta$ state, the former has more similarities to the $+\beta$ state (c.f. Fig. 1d). These theoretical results indicate that the different spatial experimental distributions of the $+\beta$ and $-\beta$ states in Fig. 1d can be explained by supposing that they correspond to two different YSR states of

$d_{x^2-y^2}$ and d_{xz} orbital character which overlap within the experimental energy resolution, rather than to a single YSR state. The two YSR peaks also overlap in the theoretical calculations if a larger imaginary part is chosen for the energy, corresponding to a higher effective temperature. Finally, note that the electron-hole asymmetries in the intensities of the calculated peaks appear to be inverted compared to the experiment. With the exception of the d_{xz} -like YSR state, each pair of peaks has a larger electron contribution above E_F (Supplementary Fig. 5a). The d_{xz} -like YSR state has a higher electron contribution below E_F which implies that this state has the strongest coupling to the substrate.

YSR states of Fe dimers. Before we continue with the investigation of Fe dimers, we consider some intuitive ideas about the most promising orientations of chains built from individual Fe atoms towards the goal of topologically gapped YSR bands. As found in previous works^{25–27,49}, enabling a sufficient hybridization of a YSR state which is already close to E_F , while, at the same time, minimizing the hybridizations of all the other YSR states far from E_F may lead to a single YSR band overlapping with E_F . Together with SOC, this can be a sufficient condition for the opening of a topologically non-trivial gap in the lowest energy band. Starting from the experimentally detected shapes and energies of the α and β YSR states (Fig. 1d) we thus regard chains along the [001] (x) direction as most promising. For this orientation, we expect weak and strong hybridizations, respectively, for the α and β YSR states which are far and close to E_F . While a manipulation of close-packed dimers along [001] turned out to be impossible, we were able to tune the system into the above

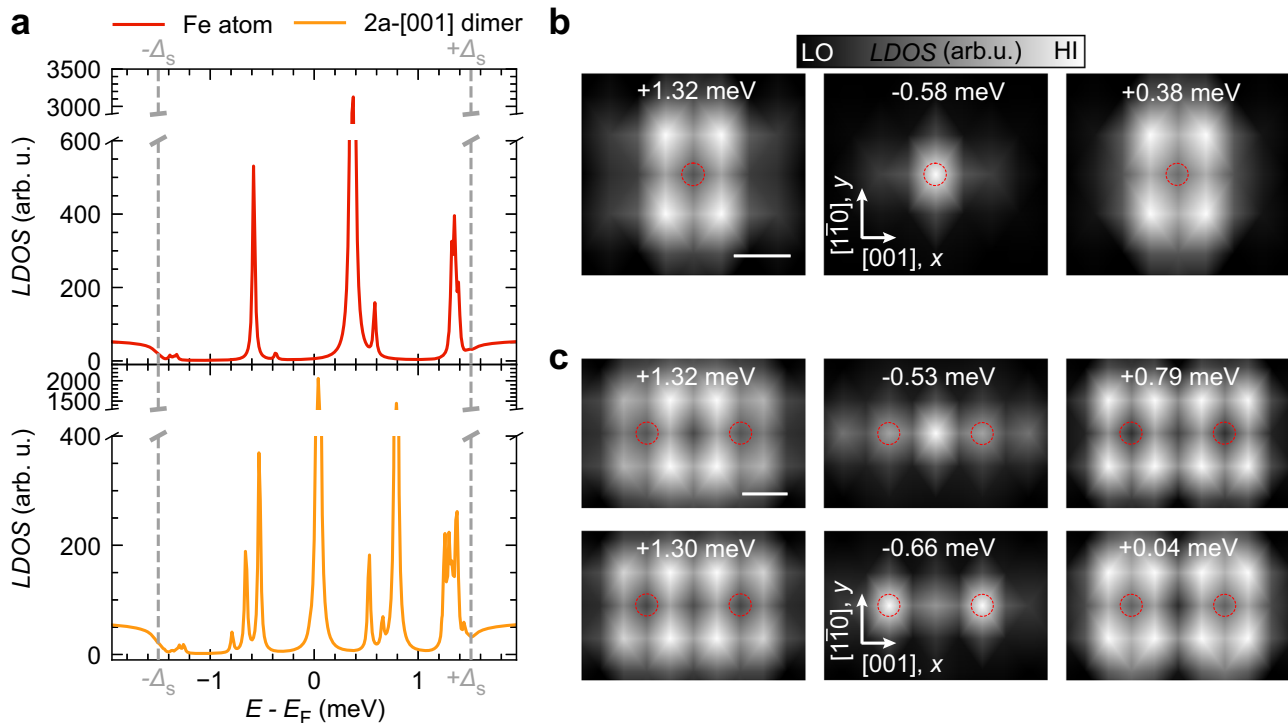


Figure 2 Calculated Yu-Shiba-Rusinov (YSR) states of Fe atoms and dimers on monolayer Au on Nb(110). **a** Electron component of the local density of states (LDOS) in arbitrary units (arb. u.) of the single Fe atom (red curve) and the ferromagnetic $2a - [001]$ dimer (orange curve). Gray dashed vertical lines indicate the superconducting gap of the substrate Δ_s . **b** Spatial distributions of the three YSR peaks of the Fe atom with the highest intensities visible in the red curve of (**a**). **c** Spatial distributions of the six YSR peaks of the ferromagnetic (FM) $2a - [001]$ dimer with the highest intensities visible in the orange curve of (**a**). The energies are indicated in the top of the panels of (**b**) and (**c**). Red dashed circles indicate the positions of Fe atoms and the white scale bars correspond to a distance of a .

conditions using dimers with a distance of $2a$ along $[001]$ ($a = 329.4$ pm, see STM image in Fig. 1e). A dI/dV spectrum measured above the center of the dimer as well as constant-contour maps of the spatial distributions of the three evident states are displayed in the orange curve of Fig. 1c and in Fig. 1e, respectively. In this configuration, the $\pm\alpha$ YSR states of the two atoms do not overlap significantly such that they do not split into hybridized states, but only slightly shift in energy. In contrast, the $\pm\beta$ YSR states of the two atoms strongly overlap, and split into an energetically higher one with a clear nodal line in the center between both impurities ($\pm\beta_a$) and another energetically lower one with an increased intensity in the center ($\pm\beta_s$).

These experimental conclusions are corroborated by our calculations (Fig. 2a, orange curve, and Fig. 2c). Apparently, all five pairs of single-atom YSR states are split, as expected from previous experimental and theoretical studies^{28,50}. Although based on the orbital decomposition it is possible to separate all of the ten pairs (Supplementary Note 6 and Supplementary Fig. 6), the splitting of the three YSR states contributing to the α YSR state is particularly small, in accordance with the experiment, which makes it hard to resolve them in the total LDOS. In Fig. 2c we plot the LDOS maps of the six most relevant peaks in Fig. 2a. We find that the very weakly split d_{yz} YSR states at +1.32 meV and +1.30 meV, which are assigned to the experimental α YSR state, appear with an almost identical shape as the single atom d_{yz} YSR state (cf. Fig. 2b). In contrast, the $d_{x^2-y^2}$ and d_{xz} YSR states strongly split into states with larger (at +0.79 meV and -0.53 meV) and smaller (at +0.04 meV and -0.66 meV) intensities in the center between both impurities, and are thus associated with the experimental $\pm\beta_s$ and $\pm\beta_a$ YSR states, respectively. We thus conclude that, while the α YSR states

hybridize only very weakly, the β YSR states hybridize strongly and split into states which resemble anti-symmetric and symmetric linear combinations of the single atom YSR states⁵¹⁻⁵³, which can be seen as a prerequisite for band formation from the hybridizing β YSR states.

Gapless YSR band in ferromagnetic Fe chains on Au monolayer. Having identified a promising orientation and interatomic spacing from the investigation of the single atom and the dimer above, we move on to study artificial chains with the same interatomic separation, called $2a - [001]$ chains in the following. A sketch illustrating this geometry and an STM image of a nine Fe atoms long Fe_9 $2a - [001]$ chain are shown in Fig. 3a and b. Spin-polarized measurements of a Fe_{16} $2a - [001]$ chain indicate that the atoms in this chain configuration prefer ferromagnetic alignment (Supplementary Note 3 and Supplementary Fig. 3). This is also supported by our DFT calculations (Supplementary Note 5). We found that the DMI is around 10% of the Heisenberg exchange interaction in the dimer (Supplementary Table 1). Although this is not particularly weak, the SOC in the Au layer additionally induces a very strong out-of-plane on-site anisotropy, which prevents the formation of spin-spirals and stabilizes a normal-to-plane ferromagnetic spin structure.

A dI/dV line profile (see Methods) was measured in the center of such a chain along its main axis and is plotted in Fig. 3a alongside the acquired stabilization height profile. The first apparent characteristic of this measurement is the modulation of every feature with the interatomic spacing of $2a$ in these chains, which is also visible in the height profile. It should be emphasized that this is not a feature of the chains' in-gap band structure but is just due to the lattice-periodic part of the wave function.

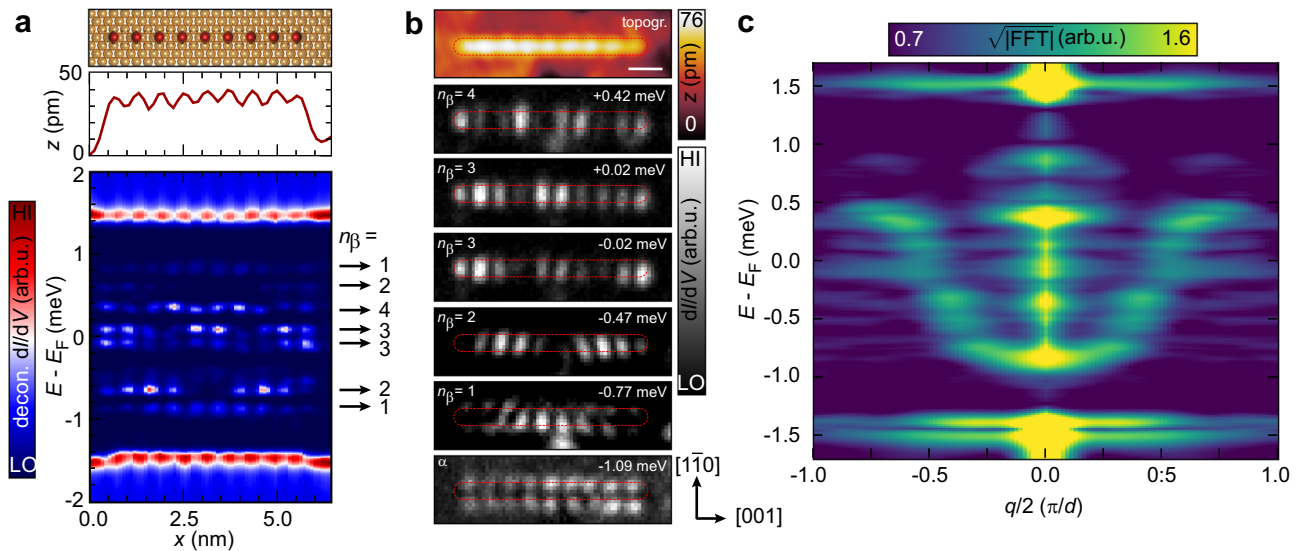


Figure 3 Measured dispersion of Bogoliubov-de Gennes (BdG) quasiparticles in Fe chains on Au monolayer. **a** Deconvoluted dI/dV line profile (named decon. dI/dV , given in arbitrary units, arb. u.) and corresponding topographic line profile (z given in picometers, pm) measured along the longitudinal axis (x) of a Fe_9 $2a - [001]$ chain, as illustrated in the sketch at the top, where the red spheres depict the Fe atoms and the golden spheres the surface Au atoms. Black arrows mark the energies in the deconvoluted dI/dV line profile at which n_β maxima as indicated are observed along the chain. The subscript of this label refers to the orbital origin of this state ($V_{\text{stab}} = 6$ mV, $I_{\text{stab}} = 1$ nA, $V_{\text{mod}} = 20$ μV). **b** The colored topography image (topogr.) shows a scanning tunneling microscope (STM) image of a Fe_9 $2a - [001]$ chain and the grayscale images are dI/dV maps of this chain, obtained at energies indicated in the top right corner of each panel. The maps are labeled by n_β in a similar fashion as the states in **(a)**. The dashed red elliptical circumferences mark the spatial extent of the chain in the STM image. The white scale bar represents a length of 1 nm ($V_{\text{stab}} = -6$ mV, $I_{\text{stab}} = 1$ nA, $V_{\text{mod}} = 20$ μV). **c** Averaged energy-wise one-dimensional fast Fourier transforms (1D-FFT) obtained from dI/dV line profiles of Fe_N $2a - [001]$ chains with lengths N ranging from seven to fourteen atoms. Prior to the 1D-FFT, the spectra were deconvoluted. All dI/dV line profiles were obtained with the following parameters: $V_{\text{stab}} = 6$ mV, $I_{\text{stab}} = 1$ nA, $V_{\text{mod}} = 20$ μV .

However, we find additional states with different well-defined numbers of maxima at increasing energy and also very close to E_F as indicated by the labels n_β ($n_\beta - 1$) for the numbers of maxima (nodes). Note that for most of these states we can identify the particle-hole partners occurring on the other side of E_F with the same energetic distance to E_F and equal numbers of maxima and nodes (see, e.g., $n_\beta = 1, 2, 3$ in Fig. 3a and additional examples in Supplementary Fig. 4). However, they mostly have much smaller intensities and may overlap with states of other n_β such that they are barely visible for some of the cases (e.g., $n_\beta = 4$). These pairs of states can thus be assigned to confined Bogoliubov-de Gennes (BdG) quasiparticles residing in a YSR band induced by the finite magnetic chain in the superconductor²⁵. To determine the orbital origin of these states, we show dI/dV maps (see Methods) of the Fe_9 $2a - [001]$ chain in Fig. 3b. We find that the confined BdG states identified before in Fig. 3a are localized inside the spatial extent of the chain deduced from the STM image (dashed red elliptical circumference). We assign those states to a band formed by the strong hybridization of the $\pm\beta$ YSR states of the single adatoms as they are expected to be largely localized along the longitudinal axis of the chain. Additionally, there is a state at a similar energy as the single adatom and dimer $\pm\alpha$ YSR states around ± 1.09 meV. This state has exactly as many maxima as there are atoms in the chain, namely 9, which are spatially localized along both sides of the chain with a similar distance to the chain axis as the lobes of the single adatom and dimer's $\pm\alpha$ YSR states (cf. Fig. 1d and e). Therefore, we assign this state to the very weakly hybridizing $\pm\alpha$ YSR states of the single atom. The state is not observed in the dI/dV line profile of Fig. 3a due to its nodal line along the longitudinal chain axis.

In order to measure the dispersion of the confined BdG states from the β YSR band, we collect similar dI/dV line profiles as the one in Fig. 3a of defect-free chains for lengths ranging from $N = 7$

to $N = 14$ atoms ($\text{Fe}_7 - \text{Fe}_{14}$, see Supplementary Note 4 and Supplementary Fig. 4). It can be observed that the confined BdG quasiparticle states shift in energy as a function of the length $L = N \cdot d = N \cdot 2a$ of the chain, as expected from the length-dependent interference condition

$$q = |q| = \pm \frac{2\pi n}{L} \quad (1)$$

where n is an integer and $|q|$ is the length of the BdG quasiparticle scattering vector²⁵. For particular chain lengths, the confined BdG quasiparticle states can be located very close to E_F (c.f. Fe_8 and Fe_{10} in Supplementary Fig. 4). We perform one-dimensional fast Fourier transforms (1D-FFT) of the columns of the dI/dV line profiles at fixed energy E averaging all data sets taken for chains of multiple lengths, and thereby obtain the dispersion of the scattering vectors $E(q)$ (Fig. 3c). This dispersion is closely linked to the β YSR band structure. We find that this band has an approximately parabolic dispersion ranging from -0.9 meV at $q/2 = 0$ to $+0.5$ meV at $q/2 = \pi/d$. Note that, as already discussed for the dI/dV line profiles above, the particle-hole partner of this band has a much lower intensity. It is only visible around the Brillouin zone center ($q/2 = 0$) in our measurements. Most importantly, the β YSR band smoothly crosses E_F without any indications of a minigap opening.

An overall similar behaviour is found using our ab-initio framework. We performed calculations for $2a - [001]$ chains of lengths ranging from 9 to 19 Fe atoms with ferromagnetic spin alignment (Supplementary Note 7 and Supplementary Fig. 7). Exemplarily, the calculated LDOS along a Fe_9 chain is shown in Fig. 4a and can be directly compared to the measured line profile in Fig. 3a. The band formation of the YSR states can clearly be observed in a wide range of the substrate gap in the form of LDOS lines with a well-defined number of maxima along the chain as

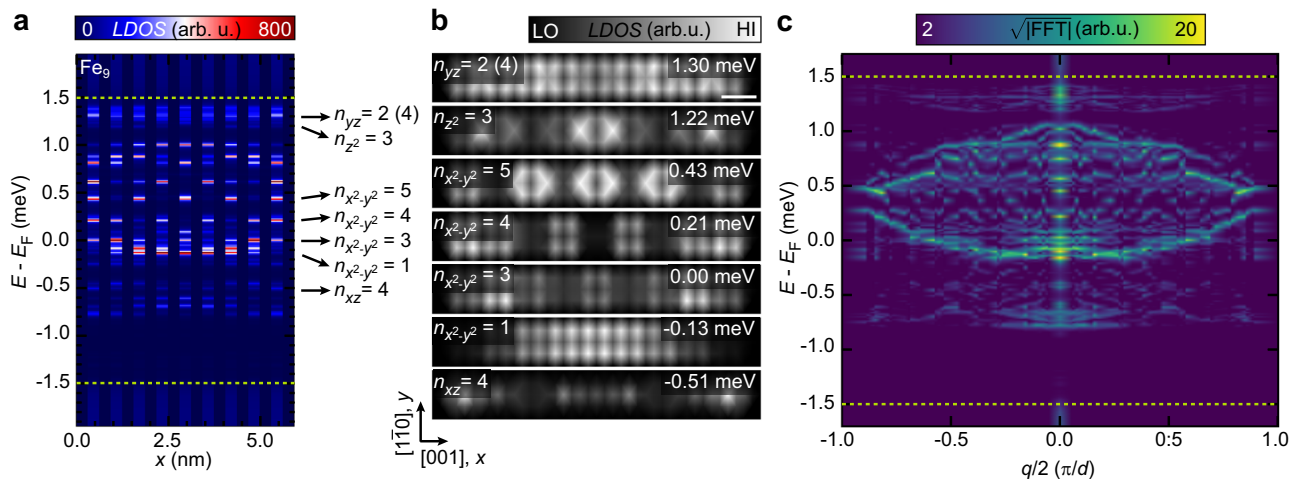


Figure 4 Calculated dispersion of Bogoliubov-de Gennes (BdG) quasiparticles in ferromagnetic Fe chains on Au monolayer. **a** Electron component of the local density of states (LDOS, given in arbitrary units, arb. u.) extracted along the longitudinal axis (x) of a ferromagnetic Fe₉ 2a – [001] chain, calculated on the Fe and the vacuum sites in between. **b** Spatial distributions of the LDOS evaluated in the first vacuum layer above the chain. Energies are indicated in the top right corners of each panel, while the numbers of maxima and the orbital origins of the states are indicated in the top left corners. They correspond to the states marked by the same arrows and numbers in (a). The n_{yz} state has two dominant Fourier components $n_{yz} = 2$ and $n_{yz} = 4$, where the former is dominating. The white scale bar has a length of $2a$. **c** Dispersion of scattering wave vectors extracted by the one-dimensional fast Fourier transforms (1D-FFT) from the calculated LDOSs of ferromagnetically coupled Fe_N 2a – [001] chains and averaged for lengths N of 9, 11, 13, 14, 17 and 19 atoms (Supplementary Fig. 7). The green dashed lines in panels (a) and (c) indicate the energy gap of the superconducting substrate.

indicated in the figure. In Fig. 4b we present the corresponding spatial distributions of the LDOS of the Fe₉ chain in the form of two-dimensional maps for a selection of confined BdG states with the indicated dominant orbital characters and numbers of maxima (see the Methods section for calculation details). The states closest to the substrate’s coherence peaks with $n_{yz} = 2$ (and admixed $n_{yz} = 4$) and $n_{z^2} = 3$ maxima have d_{yz} and d_{z^2} orbital characters, respectively. They reside in a very narrow band formed by the weakly interacting α YSR states of the Fe atoms (Fig. 2), which explains the low dispersion of this band. On the contrary, wide bands are formed by the strong hybridization of the β YSR states, i.e. a $d_{x^2-y^2}$ YSR band (between -0.2 meV and $+1.1$ meV) having high intensities on both sides along the longitudinal axis of the chain and a d_{xz} YSR band (between -0.8 meV and 0 meV) characterized by high intensities between the atoms of the chain (Fig. 4a, b). In order to deduce the dispersions of these YSR bands from the theoretical calculations, we applied the same 1D-FFT method as in the experiment²⁵, and averaged over chains containing 9, 11, 13, 14, 17 and 19 Fe atoms (Supplementary Fig. 7). The result is plotted in Fig. 4c and can be compared to the experimental dispersion in Fig. 3c. The most characteristic, broad bands are the $d_{x^2-y^2}$ and d_{xz} YSR bands between -0.2 meV and 1.1 meV and between -0.8 and 0 meV, respectively. While the energy range of the d_{xz} YSR band agrees reasonably well with that of the experimental β band, the $d_{x^2-y^2}$ YSR band is probably not detected significantly in the experimental data (Fig. 3c). The latter might be explained by the small intensity of the experimental $+\beta$ state (Fig. 1c) which is not reproduced by the calculations (Fig. 2a). Most importantly, the theoretical study confirms the lack of a detectable minigap at E_F in the YSR bands.

Minigap and end states in spin spiral Fe chains on Au monolayer. At first sight, the missing minigap seems surprising. For similar ferromagnetic chains on the lighter substrates

Nb(110) and Ta(110) there are already clear indications for the openings of topological minigaps^{25,54}. It is widely accepted that topological minigaps hosting MBS can open in the quasiparticle spectrum of one-dimensional helical spin systems being proximity-coupled to a conventional s -wave superconductor^{15,16,19,55}. For ferromagnetic chains, this phenomenon has been attributed to a Rashba-type SOC induced by the substrate⁵⁶, which is equivalent to a spin spiral structure without SOC in a single-band tight-binding model⁵⁷. As outlined in the introduction above, the heavier material Au is well known to exhibit large SOC^{5,30}. However, as our experiments and calculations show, it obviously does not induce a spin-spiral state in the Fe chain, and likewise does not induce a SOC of sufficient strength in the YSR bands of the ferromagnetic chain to open a detectable minigap. In order to trace whether we can still force the system into a state with a large topological gap Δ_{ind} just by artificially imposing a suitable non-collinear spin state onto the chain, we performed calculations for the same chains as before, but now imposing a helical spin spiral state (Fig. 5, Supplementary Note 8, and Supplementary Fig. 8). The configuration of the spin spiral was such that the first Fe site had its spin pointing along the positive z direction and then each spin is rotated by 90° around the chain axis when moving along the chain (Fig. 5a). Indeed, there are two significant features which emerge in the LDOS of the spin-spiral chain with 19 iron atoms (Fig. 5b), which were absent in the LDOS of the ferromagnetic chain (Fig. 4a). First, a minigap at E_F opens up between -0.22 meV and $+0.22$ meV. Second, inside this minigap a single state can be observed at E_F with a pronounced intensity localized at the ends of the chain. This state has an electron-hole ratio of 1 and is robust against the variation of the chain length from 9 to 19 atoms as illustrated in Fig. 5b and Supplementary Fig. 8. Note, however, that this state slightly splits off from E_F for particular chain lengths (see Supplementary Note 8 and Supplementary Fig. 8b and d), which is a well-known finite-size effect of MBS in spin chains on superconductors²⁶. The strongly different spatial

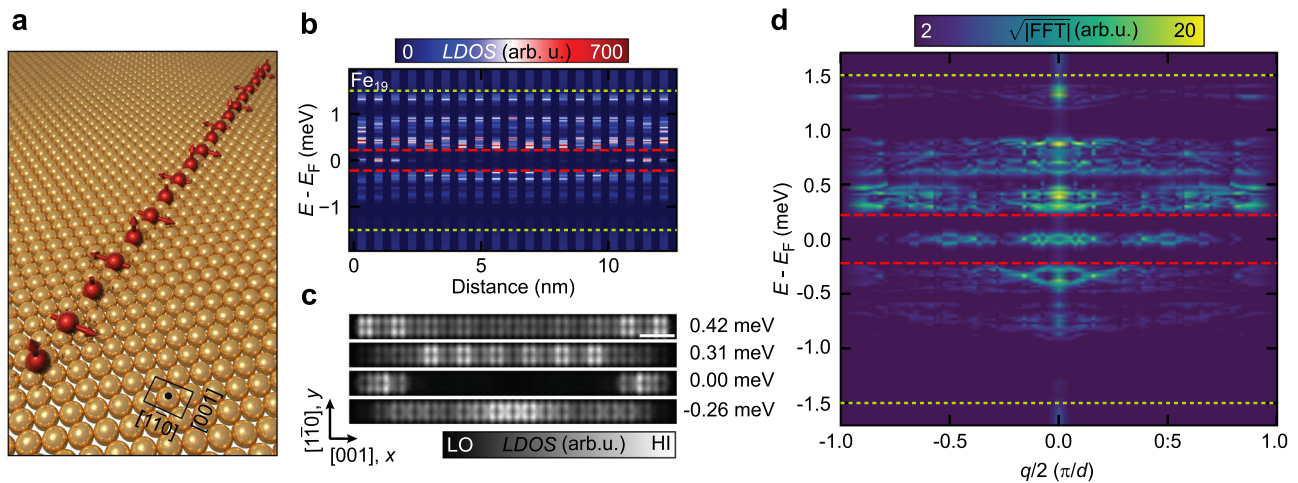


Figure 5 Minigap and Majorana bound state (MBS) enforced by helical spin spirals in Fe chains on Au monolayer. **a** Illustration of the helical spin spiral state (red arrows) with a rotation angle of 90° of a chain containing 19 Fe atoms (red spheres) assembled on the lattice of Au atoms (golden spheres) on Nb(110) (not visible). **b** Electron component of the local density of states (LDOS, given in arbitrary units, arb. u.) extracted along the longitudinal axis (distance x) of a $\text{Fe}_{19} 2a - [001]$ chain in the helical spin spiral state shown in panel (a). **c** The spatial distributions of the LDOS evaluated in the first vacuum layer above the $\text{Fe}_{19} 2a - [001]$ chain at the energies indicated to the right of each panel. **d** Dispersion of scattering wave vectors averaged from the one-dimensional fast Fourier transforms (1D-FFT) of the calculated LDOSs of the $\text{Fe}_N 2a - [001]$ chains including $N = 9, 11, 13, 14, 17$ and 19 Fe atoms (Supplementary Fig. 8). The green and red dashed lines in (b) and (d) indicate the substrate gap and the minigap, respectively.

LDOS distribution of the almost-zero-energy state inside the minigap compared to that of some exemplary higher-energy states outside the minigap is further illustrated in Fig. 5c. The former is localized over a few atoms at the two ends of the chain, while the latter states outside the minigap are extended along the whole chain. It should be mentioned that all these states, both the zero-energy one as well as those outside of the minigap show the same orbital character, indicating that the minigap emerges from the $d_{x^2-y^2}$ YSR states of the adatom. The induced minigap of $2\Delta_{\text{ind}} = 0.44$ meV width and the narrow spectral weight around E_F stemming from the zero-energy end states are also clearly visible in the dispersion of the scattering wave vectors deduced from the averaged 1D-FFTs of the LDOSs of chains of different lengths (Fig. 5d). Thus, the calculations show evidence for the formation of a topological, most probably p -wave-like, minigap which hosts a MBS, if the Fe chain on Au(111) is forced into a helical spin spiral state, indicating that the absence of the non-collinear ground state is the limiting factor of this experimental system.

Conclusions

In summary, our combined experimental and theoretical investigation shows that in contrast to what might be suggested by simplified tight-binding models^{56,57}, a strong substrate SOC alone generally is not a sufficient condition for the opening of a topological minigap in a ferromagnetic chain in contact to an s -wave superconductor, since the SOC has to exist in the lowest-energy YSR band. In fact, first-principles calculations of the magnetic interaction parameters in ultrathin film systems have demonstrated that also the connection between the formation of a spin-spiral state and SOC is considerably more complicated. In particular, the DMI preferring a non-collinear spin alignment is typically weak when a $3d$ transition metal is deposited on a Au surface compared to other $5d$ substrates^{58–60}, which may be tentatively attributed to the fully occupied $5d$ band of Au having a reduced effect on the DMI. Proximity to a Au layer is known to give rise to strong Heisenberg exchange interactions and anisotropy³⁴ in the magnetic layer instead, both of which prefer a collinear spin alignment and the latter being induced by the SOC.

Our results indicate that, similarly to the competition between DMI and anisotropy terms in the formation of non-collinear spin structures, the role of SOC may be more complex for inducing topological superconductivity in the YSR bands of ferromagnetic spin chains.

Our study proves that it is experimentally possible to grow proximitized ultrathin heavy-metal layers on a superconductor with a large T_c that can be used as a substrate for the deposition of transition-metal atoms and to construct defect-free one-dimensional structures with an excellent quality, enabling the tailoring of YSR bands. Furthermore, we presented an ab-initio method that accurately reproduces the main LDOS features observed in the experiments. Our work thus demonstrates the theoretical feasibility of an ab-initio screening of other combinations of transition-metal chains on heavy-metal thin films on bulk superconductors in order to find the optimal conditions for the opening of a large topological minigap.

Methods

STM and STS measurements. The experiments were performed in a custom home-built ultra-high vacuum system, equipped with an STM setup, which was operated at a temperature of 320 mK⁶¹. STM images were obtained by applying a bias voltage V_{bias} to the sample upon which the tip-sample distance is controlled by a feedback loop such that a constant current I is achieved. dI/dV spectra were obtained in open feedback mode after stabilizing the tip at $V_{\text{stab}} = 6$ mV and $I_{\text{stab}} = 1$ nA using a standard lock-in technique with an AC voltage $V_{\text{mod}} = 20 \mu\text{V}$ (rms value) of frequency $f_{\text{mod}} = 4142$ Hz added to the ramped V_{bias} . If other stabilization parameters were used for a particular measurement, it is indicated in the respective figure caption. dI/dV maps were obtained by measuring dI/dV spectra on a predefined spatial grid, which was positioned over the structure of interest, and selecting a slice at a given voltage. Typical measurement parameters are the same as for individual dI/dV spectra. dI/dV line profiles are measured similarly to dI/dV maps, with the exception that the spatial grid is one-dimensional. Constant-contour maps were obtained by repeated scanning of individual lines of STM images. First, each line is measured as it would be the case in a regular STM image. The z -signal of this sweep is saved. Then, the feedback is turned off, the bias voltage V_{bias} is set to a predefined value of interest, and for the next sweep on the same scan line the dI/dV signal is measured while restoring the previously recorded z -signal.

A mechanically sharpened and in-situ flashed (50 W) bulk Nb tip was used for all measurements. While the usage of a superconducting tip is a crucial factor for obtaining a very good energy resolution, it has the downside that the dI/dV spectra are convolutions of the tip and sample DOSs. However, we can determine the superconducting gaps of the tip and the sample, and deconvolute the dI/dV spectra.

This process is described in Supplementary Note 2 and is performed for every spectrum in the main manuscript.

Sample preparation. A Nb(110) single crystal with a purity of 99.99% was transferred into the ultra-high vacuum chamber. The sample was cleaned by cycles of Ar ion sputtering and flashes up to 2400 °C, which results in a clean surface with only few oxygen impurities remaining⁶². We established flashing parameters which clean the surface of oxygen, and checked the results by STM. Once this cleaning procedure was reproducible with the given parameters, we evaporated Au from an e-beam evaporator (EFM3 by FOCUS GmbH) equipped with a Au rod (99.99% purity). Following this procedure, we achieved flat and spatially extended films (Fig. 1a).

Fe was evaporated onto the surface from a carefully outgassed Fe rod using a second e-beam evaporator while keeping the sample temperature below $T = 10$ K to avoid clustering and diffusion and thus achieve a random distribution of single Fe adatoms (Fig. 1b). From Supplementary Note 1, we conclude that the Au film grows pseudomorphically and that the Fe atoms are adsorbed in the fourfold coordinated hollow sites in the center of four Au atoms. This is further supported by the similarity of the spatial distributions of the YSR states of the Fe/Au/Nb(110) system compared to the Mn/Nb(110) system²⁸.

STM tip-induced atom manipulation^{24,41} is used to position individual Fe atoms and construct artificial structures, such as dimers and chains. The structures built in this study have sufficient interatomic spacing to unambiguously identify the positions of the individual atoms forming the structure using STM images. We restrict the investigations here to Fe atoms positioned on the first monolayer of Au. Fe atoms on the first and second monolayer can easily be distinguished by their apparent height. In the topmost part of Fig. 1b one can see that an Fe atom on the second monolayer appears as a bright spherical protrusion, while an Fe atom on the first monolayer is more shallow and has a relatively irregular shape. Thus, we can be sure that all of the experiments were carried out on the first monolayer.

First-principles calculations. The calculations were performed in terms of the Screened Korrington-Kohn-Rostoker method (SKKR), based on a fully relativistic Green's function formalism by solving the Dirac equation for the normal state³⁴ and the DBdG equation for the superconducting state within multiple scattering theory (MST)^{50,63}. The impurities are included within an embedding scheme⁶⁴, being an efficient method to address the electronic and magnetic properties or the in-gap spectra of real-space atomic structures without introducing a supercell. The system consists of seven atomic layers of Nb, a single atomic layer of Au and four atomic layers of vacuum between semi-infinite bulk Nb and semi-infinite vacuum. The Fe adatoms are placed in the hollow position in the vacuum above the Au layer and relaxed towards the surface by 21%, while the top Au layer is also relaxed inwards by 2%. The relaxations are obtained from total-energy minimization in a VASP^{65–67} calculation for a single Fe adatom and are used for the dimer and all the chains. For the potentials we employ the atomic sphere approximation (ASA), the normal state is calculated self-consistently in the local density approximation (LDA) as parametrized by Vosko et al.⁶⁸ The partial waves within MST are treated with an angular momentum cutoff of $\ell_{\max} = 2$. In the self-consistent normal state calculations we used a Brillouin zone (BZ) integration with 253 k points in the irreducible wedge of the BZ and a semicircular energy contour on the upper complex semiplane with 16 points for energy integration. In order to take into account charge relaxation around the magnetic sites, the single impurity and the $2a - [001]$ dimer are calculated by including a neighborhood containing 48 and 84 atomic sites, respectively, corresponding to a spherical radius of $r = 1.66a$. The atomic chains are calculated with a somewhat smaller neighborhood corresponding to 2 atomic shells or a spherical radius of $r = 1.01a$ around the Fe atoms. This way our largest atomic cluster in the calculation with 19 Fe chain atoms contained 339 atomic sites. After having obtained the self-consistent potentials in the normal state, the superconducting state is simulated within single-shot calculations by solving the DBdG equation with the experimental band gap used as the pairing potential in the Nb layers⁵⁰. In the case of the single impurity and the dimer, the BZ integration for the host Green's function is performed by using the same k mesh as for the normal state, but in order to achieve convergence for the chains we had to increase the number of k points up to 1891 in the irreducible wedge of the BZ. A sufficient energy resolution of the LDOS in the superconducting gap is acquired by considering 301 energy points between ± 1.95 meV with an imaginary part of $13.6 \mu\text{eV}$ related to the smearing of the resulting LDOS. Both the electron and the hole components of the LDOS are calculated, but in this paper we present only the electron part leading to the asymmetry of the spectrum as also seen in the experiments. Due to the ASA used in our method we obtain the LDOS for each atomic site of the cluster averaged inside the atomic spheres. The orbital resolution of the YSR states can be determined based on the orbital-resolved LDOS of the Fe atoms. Since the canonical d orbitals hybridize due to the symmetry of the cluster and due to SOC, we assign the labels based on the orbital which has the largest contribution to the given peak in the LDOS. In addition, in order to mimic the constant-contour maps in the experiments, we evaluate the spatial distribution of the LDOS. These LDOS maps are taken from

the first vacuum layer above the surface in which the magnetic atoms are embedded, reflecting the orbital characteristics obtained from the resolution of the LDOS of the Fe atoms. In order to better reproduce the experimental constant-contour maps taken from the vacuum region, the LDOSs of the magnetic sites are replaced by the average LDOS over the two vacuum sites (empty spheres) closest to them in the layer above. To get a continuous picture for the LDOS maps we applied an interpolation⁶⁹ scheme on the data calculated as described above.

Data availability

The authors declare that all relevant data supporting the findings of this study are available within the paper and its Supplementary Information files.

Code availability

The analysis codes that support the findings of the study are available from the corresponding author on reasonable request.

Received: 1 September 2022; Accepted: 6 April 2023;

Published online: 24 April 2023

References

- Soumyanarayanan, A., Reyren, N., Fert, A. & Panagopoulos, C. Emergent phenomena induced by spin-orbit coupling at surfaces and interfaces. *Nature* **539**, 509–517 (2016).
- Dzyaloshinsky, I. A thermodynamic theory of “weak” ferromagnetism of antiferromagnetics. *J. Phys. Chem. Solids* **4**, 241–255 (1958).
- Moriya, T. New mechanism of anisotropic superexchange interaction. *Phys. Rev. Lett.* **4**, 228–230 (1960).
- Bode, M. et al. Chiral magnetic order at surfaces driven by inversion asymmetry. *Nature* **447**, 190–193 (2007).
- LaShell, S., McDougall, B. A. & Jensen, E. Spin splitting of an Au(111) surface state band observed with angle resolved photoelectron spectroscopy. *Phys. Rev. Lett.* **77**, 3419–3422 (1996).
- Ast, C. R. et al. Giant spin splitting through surface alloying. *Phys. Rev. Lett.* **98**, 186807 (2007).
- Fu, L. & Kane, C. L. Topological insulators with inversion symmetry. *Phys. Rev. B* **76**, 045302 (2007).
- Hasan, M. Z. & Kane, C. L. Colloquium: topological insulators. *Rev. Mod. Phys.* **82**, 3045–3067 (2010).
- Fu, L. & Kane, C. L. Superconducting proximity effect and Majorana fermions at the surface of a topological insulator. *Phys. Rev. Lett.* **100**, 096407 (2008).
- Lutchyn, R. M., Sau, J. D. & Sarma, S. D. Majorana fermions and a topological phase transition in semiconductor-superconductor heterostructures. *Phys. Rev. Lett.* **105**, 077001 (2010).
- Potter, A. C. & Lee, P. A. Topological superconductivity and Majorana fermions in metallic surface states. *Phys. Rev. B* **85**, 094516 (2012).
- Mourik, V. et al. Signatures of Majorana fermions in hybrid superconductor-semiconductor nanowire devices. *Science* **336**, 1003–1007 (2012).
- Kjaergaard, M., Wölms, K. & Flensberg, K. Majorana fermions in superconducting nanowires without spin-orbit coupling. *Phys. Rev. B* **85**, 020503 (2012).
- Klinovaja, J., Stano, P., Yazdani, A. & Loss, D. Topological superconductivity and Majorana fermions in RKKY systems. *Phys. Rev. Lett.* **111**, 186805 (2013).
- Pientka, F., Glazman, L. I. & von Oppen, F. Topological superconducting phase in helical Shiba chains. *Phys. Rev. B* **88**, 155420 (2013).
- Nadj-Perge, S., Drozdov, I. K., Bernevig, B. A. & Yazdani, A. Proposal for realizing Majorana fermions in chains of magnetic atoms on a superconductor. *Phys. Rev. B* **88**, 020407 (2013).
- Nadj-Perge, S. et al. Observation of Majorana fermions in ferromagnetic atomic chains on a superconductor. *Science* **346**, 602–607 (2014).
- Ruby, M. et al. End states and subgap structure in proximity-coupled chains of magnetic adatoms. *Phys. Rev. Lett.* **115**, 197204 (2015).
- Kim, H. et al. Toward tailoring Majorana bound states in artificially constructed magnetic atom chains on elemental superconductors. *Sci. Adv.* **4**, eaar5251 (2018).
- Freedman, M., Kitaev, A., Larsen, M. & Wang, Z. Topological quantum computation. *Bull. Am. Math. Soc.* **40**, 31–38 (2002).
- Schneider, L. et al. Controlling in-gap end states by linking nonmagnetic atoms and artificially-constructed spin chains on superconductors. *Nat. Commun.* **11**, 4707 (2020).

22. Pientka, F., Peng, Y., Glazman, L. & von Oppen, F. Topological superconducting phase and Majorana bound states in Shiba chains. *Phys. Scr.* **T164**, 014008 (2015).
23. Mier, C. et al. Atomic manipulation of in-gap states in the β -Bi₂Pd superconductor. *Phys. Rev. B* **104**, 045406 (2021).
24. Eigler, D. M. & Schweizer, E. K. Positioning single atoms with a scanning tunnelling microscope. *Nature* **344**, 524–526 (1990).
25. Schneider, L. et al. Topological Shiba bands in artificial spin chains on superconductors. *Nat. Phys.* **17**, 943–948 (2021).
26. Schneider, L. et al. Precursors of Majorana modes and their length-dependent energy oscillations probed at both ends of atomic Shiba chains. *Nat. Nanotechnol.* **17**, 384–389 (2022).
27. Küster, F. et al. Non-Majorana modes in diluted spin chains proximitized to a superconductor. *Proc. Natl. Acad. Sci. U.S.A.* **119**, e2210589119 (2022).
28. Beck, P. et al. Spin-orbit coupling induced splitting of Yu-Shiba-Rusinov states in antiferromagnetic dimers. *Nat. Commun.* **12**, 2040 (2021).
29. Ding, H. et al. Tuning interactions between spins in a superconductor. *Proc. Natl. Acad. Sci. U.S.A.* **118**, e2024837118 (2021).
30. Henk, J., Hoesch, M., Osterwalder, J., Ernst, A. & Bruno, P. Spin-orbit coupling in the L-gap surface states of Au(111): spin-resolved photoemission experiments and first-principles calculations. *J. Phys.: Condens. Matter* **16**, 7581–7597 (2004).
31. Bergman, G. Influence of spin-orbit coupling on weak localization. *Phys. Rev. Lett.* **48**, 1046–1049 (1982).
32. Bihlmayer, G., Koroteev, Y., Echenique, P., Chulkov, E. & Blügel, S. The Rashba-effect at metallic surfaces. *Surf. Sci.* **600**, 3888–3891 (2006).
33. Marchenko, D. et al. Giant Rashba splitting in graphene due to hybridization with gold. *Nat. Commun.* **3**, 1232 (2012).
34. Szunyogh, L., Újfalussy, B. & Weinberger, P. Magnetic anisotropy of iron multilayers on Au(001): first-principles calculations in terms of the fully relativistic spin-polarized screened KKR method. *Phys. Rev. B* **51**, 9552–9559 (1995).
35. Lounis, S., Bringer, A. & Blügel, S. Magnetic adatom induced skyrmion-like spin texture in surface electron waves. *Phys. Rev. Lett.* **108**, 207202 (2012).
36. Cardias, R. et al. Magnetic and electronic structure of Mn nanostructures on Ag(111) and Au(111). *Phys. Rev. B* **93**, 014438 (2016).
37. Manna, S. et al. Signature of a pair of Majorana zero modes in superconducting gold surface states. *Proc. Natl. Acad. Sci. U.S.A.* **17**, 8775–8782 (2019).
38. Ruckman, M. W. & Jiang, L.-Q. Growth and thermal stability of Ag or Au films on Nb(110). *Phys. Rev. B* **38**, 2959–2966 (1988).
39. Choi, D.-J. et al. Influence of magnetic ordering between Cr Adatoms on the Yu-Shiba-Rusinov states of the β -Bi₂Pd superconductor. *Phys. Rev. Lett.* **120**, 167001 (2018).
40. Küster, F., Brinker, S., Lounis, S., Parkin, S. S. P. & Sessi, P. Long range and highly tunable interaction between local spins coupled to a superconducting condensate. *Nat. Commun.* **12**, 6722 (2021).
41. Strosio, J. A. & Celotta, R. J. Controlling the dynamics of a single atom in lateral atom manipulation. *Science* **306**, 242–247 (2004).
42. Csire, G., Cserti, J. & Újfalussy, B. First principles based proximity effect of superconductor–normal metal heterostructures. *J. Phys.: Condens. Matter* **28**, 495701 (2016).
43. Csire, G., Cserti, J., Túttó, I. & Újfalussy, B. Prediction of superconducting transition temperatures of heterostructures based on the quasiparticle spectrum. *Phys. Rev. B* **94**, 104511 (2016).
44. Gupta, A. K., Créton, L., Moussy, N., Pannetier, B. & Courtois, H. Anomalous density of states in a metallic film in proximity with a superconductor. *Phys. Rev. B* **69**, 104514 (2004).
45. Tomanic, T., Schackert, M., Wulfhekel, W., Sürgers, C. & v. Löhneysen, H. Two-band superconductivity of bulk and surface states in Ag thin films on Nb. *Phys. Rev. B* **94**, 220503 (2016).
46. Yazdani, A., Jones, B. A., Lutz, C. P., Crommie, M. F. & Eigler, D. M. Probing the local effects of magnetic impurities on superconductivity. *Science* **275**, 1767–1770 (1997).
47. Ruby, M., Peng, Y., von Oppen, F., Heinrich, B. W. & Franke, K. J. Orbital picture of Yu-Shiba-Rusinov multiplets. *Phys. Rev. Lett.* **117**, 186801 (2016).
48. Choi, D.-J. et al. Mapping the orbital structure of impurity bound states in a superconductor. *Nat. Commun.* **8**, 15175 (2017).
49. Liebhaber, E. et al. Quantum spins and hybridization in artificially-constructed chains of magnetic adatoms on a superconductor. *Nat. Commun.* **13**, 2160 (2022).
50. Nyári, B. et al. Relativistic first-principles theory of Yu-Shiba-Rusinov states applied to Mn adatoms and Mn dimers on Nb(110). *Phys. Rev. B* **104**, 235426 (2021).
51. Ruby, M., Heinrich, B. W., Peng, Y., von Oppen, F. & Franke, K. J. Wave-function hybridization in Yu-Shiba-Rusinov dimers. *Phys. Rev. Lett.* **120**, 156803 (2018).
52. Flatté, M. E. & Reynolds, D. E. Local spectrum of a superconductor as a probe of interactions between magnetic impurities. *Phys. Rev. B* **61**, 14810–14814 (2000).
53. Morr, D. K. & Stavropoulos, N. A. Quantum interference between impurities: creating novel many-body states in s-wave superconductors. *Phys. Rev. B* **67**, 020502 (2003).
54. Beck, P., Schneider, L., Wiesendanger, R. & Wiebe, J. Effect of substrate spin-orbit-coupling on the topological gap size of Shiba chains. Preprint at: <https://arxiv.org/abs/2205.10062> (2022).
55. Klinovaja, J. & Loss, D. Giant spin-orbit interaction due to rotating magnetic fields in graphene nanoribbons. *Phys. Rev. X* **3**, 011008 (2013).
56. Li, J. et al. Topological superconductivity induced by ferromagnetic metal chains. *Phys. Rev. B* **90**, 235433 (2014).
57. Braunecker, B., Japaridze, G. I., Klinovaja, J. & Loss, D. Spin-selective Peierls transition in interacting one-dimensional conductors with spin-orbit interaction. *Phys. Rev. B* **82**, 045127 (2010).
58. Simon, E. et al. Spin-correlations and magnetic structure in an Fe monolayer on 5d transition metal surfaces. *J. Phys. Condens. Matter* **26**, 186001 (2014).
59. Belabbes, A., Bihlmayer, G., Bechstedt, F., Blügel, S. & Manchon, A. Hund’s Rule-Driven Dzyaloshinskii-Moriya Interaction at 3d – 5d Interfaces. *Phys. Rev. Lett.* **117**, 247202 (2016).
60. Simon, E., Rózsa, L., Palotás, K. & Szunyogh, L. Magnetism of a Co monolayer on Pt(111) capped by overlayers of 5d elements: a spin-model study. *Phys. Rev. B* **97**, 134405 (2018).
61. Wiebe, J. et al. A 300mK ultra-high vacuum scanning tunneling microscope for spin-resolved spectroscopy at high energy resolution. *Rev. Sci. Instrum.* **75**, 4871–4879 (2004).
62. Odobesko, A. B. et al. Preparation and electronic properties of clean superconducting Nb(110) surfaces. *Phys. Rev. B* **99**, 115437 (2019).
63. Csire, G. et al. Relativistic spin-polarized KKR theory for superconducting heterostructures: oscillating order parameter in the Au layer of Nb/Au/Fe trilayers. *Phys. Rev. B* **97**, 024514 (2018).
64. Lazarovits, B., Szunyogh, L. & Weinberger, P. Fully relativistic calculation of magnetic properties of Fe, Co, and Ni adclusters on Ag(100). *Phys. Rev. B* **65**, 104441 (2002).
65. Kresse, G. & Furthmüller, J. Efficiency of ab-initio total energy calculations for metals and semiconductors using a plane-wave basis set. *Comput. Mater. Sci.* **6**, 15–50 (1996).
66. Kresse, G. & Furthmüller, J. Efficient iterative schemes for ab initio total-energy calculations using a plane-wave basis set. *Phys. Rev. B* **54**, 11169–11186 (1996).
67. Hafner, J. Ab-initio simulations of materials using VASP: density-functional theory and beyond. *J. Comput. Chem.* **29**, 2044–2078 (2008).
68. Vosko, S. H., Wilk, L. & Nusair, M. Accurate spin-dependent electron liquid correlation energies for local spin density calculations: a critical analysis. *Can. J. Phys.* **58**, 1200–1211 (1980).
69. Gouraud, H. Continuous shading of curved surfaces. *IEEE Trans. Computers* **100**, 623–629 (1971).

Acknowledgements

P.B., R.W., and J.W. gratefully acknowledge funding by the Deutsche Forschungsgemeinschaft (DFG, German Research Foundation) - SFB-925 - project 170620586. L.S., R.W., and J.W. gratefully acknowledge funding by the Cluster of Excellence ‘Advanced Imaging of Matter’ (EXC 2056 - project ID 390715994) of the DFG. R.W. gratefully acknowledges funding of the European Union via the ERC Advanced Grant ADMIRE (project no. 786020). B.Ny., L.R., A.L., K.P., L.Sz. and B.U. acknowledge financial support by the National Research, Development, and Innovation Office (NRDI) of Hungary under Project Nos. FK124100, K131938, K142652 and FK142601. B.Ny., L.R. and L.Sz. acknowledge support by the Ministry of Culture and Innovation and the NRDI Office within the Quantum Information National Laboratory of Hungary (Grant No. 2022-2.1.1-NL-2022-00004). B.Ny. and K.P. acknowledge the support by the ÚNKP-21-3 and the ÚNKP-21-5 New National Excellence Program of the Ministry for Innovation and Technology from the source of the National Research, Development and Innovation Fund. K.P. acknowledges the János Bolyai Research Scholarship of the Hungarian Academy of Sciences. L.R. acknowledges support by the Young Scholar Fund at the University of Konstanz.

Author contributions

P.B., L.S. and J.W. conceived the experiments. P.B. and L.S. performed the measurements and P.B. analyzed the experimental data together with J.W.. L.R. performed the VASP calculations. B.N. performed the SKKR calculations and discussed the data with L.R., A.L., K.P., L.Sz. and B.U., and A.L. also contributed to the spin model calculations. P.B. and B.N. prepared the figures and wrote the first version of the manuscript. L.S., L.R., A.L., K.P., L.Sz., B.U., J.W. and R.W. contributed to the discussions and the finalization of the manuscript.

Funding

Open Access funding enabled and organized by Projekt DEAL.

Competing interests

The authors declare no competing interests.

Additional information

Supplementary information The online version contains supplementary material available at <https://doi.org/10.1038/s42005-023-01196-y>.

Correspondence and requests for materials should be addressed to Balázs Ujfalussy or Jens Wiebe.

Peer review information *Communications Physics* thanks Geng Li and the other, anonymous, reviewer(s) for their contribution to the peer review of this work.

Reprints and permission information is available at <http://www.nature.com/reprints>

Publisher's note Springer Nature remains neutral with regard to jurisdictional claims in published maps and institutional affiliations.



Open Access This article is licensed under a Creative Commons Attribution 4.0 International License, which permits use, sharing, adaptation, distribution and reproduction in any medium or format, as long as you give appropriate credit to the original author(s) and the source, provide a link to the Creative Commons license, and indicate if changes were made. The images or other third party material in this article are included in the article's Creative Commons license, unless indicated otherwise in a credit line to the material. If material is not included in the article's Creative Commons license and your intended use is not permitted by statutory regulation or exceeds the permitted use, you will need to obtain permission directly from the copyright holder. To view a copy of this license, visit <http://creativecommons.org/licenses/by/4.0/>.

© The Author(s) 2023